Full Length Article

An effective rule for translating optimal selective laser melting processing parameters from one material to another

Hossein Ghasemi-Tabasi*, Jamasp Jhabvala, Eric Boillat, Toni Ivas, Rita Drissi-Daoudi, Roland E. Logé

Thermomechanical Metallurgy Laboratory (LMTM) – PX Group Chair, Ecole Polytechnique Fédérale de Lausanne (EPFL), CH-2002, Neuchâtel, Switzerland

ABSTRACT

Selective Laser Melting (SLM) or Laser Powder Bed Fusion (L-PBF) is the most studied laser-based additive manufacturing process for metals and alloys. One important issue in SLM is the time-consuming identification of a process window leading to quasi fully dense parts (> 99.8%), usually based on trials and errors. As some metal powders may be very expensive, and therefore not suitable for a whole battery of tests, a method to infer optimal parameters from one material to another would be highly beneficial. In this study, we use bronze as a test material for optimizing SLM parameters, before translating these parameters to red gold and 316 L steel. The concept of normalized enthalpy is used to take into account the differences in thermal and optical properties among the different materials. A translation rule is derived for the prediction of optimal processing conditions, based on the ones found for the test material. One important input for this translation rule is the powder absorptivity, which is measured at the appropriate laser wavelength and at room temperature. This approach eventually leads to the highest reported density for an additive manufactured 18-carat gold alloy (99.81% relative density), to the authors' knowledge. Finite element (FEM) simulations justify the translation rule formulation by showing the importance of the laser/powder interactions during the SLM process, leading to a finite penetration depth of the laser in the powder bed due to multiple reflections. The FEM calculations indicate that a significant part of the laser energy is directly absorbed by the powder during the manufacturing process when operating in near-optimal conditions.

1. Introduction

Additive manufacturing (AM) enables the production of intricate internal and external geometries unattainable by conventional manufacturing methods. These can be achieved with short production times and minimal custom tooling [1]. Among different AM techniques, the SLM (also called Laser Powder Bed Fusion (L-PBF)) process has received the most focus. Producing AM parts using the SLM technique requires a significant number of trials and errors cycles to optimize the process parameters, in relation with the metallic powder and its physical and chemical properties [2–4]. The process optimization is not only time consuming, but it also needs to be repeated when moving from one machine to another. The primary objective is usually to produce parts without defects such as porosity and cracks [5,6]. This objective becomes a real challenge when dealing with materials like gold, due to their high reflectivity at the standard laser wavelength (infrared). Moreover, in commercial SLM machines, a non-negligible amount of powder is needed to fill the powder supply, which makes the situation

difficult for expensive alloys. This does not prevent SLM to find an increasing interest in the jewelry and watch industries [7–13]. One way to deal with the time consuming and/or expensive trial and error procedure is to mathematically define translation rules which can predict optimum processing conditions for one material based on those found for another material.

Different strategies have been considered to define or predict optimized SLM parameters. They often determine one or several variables which are allowed to vary within a specific range of values. Some studies have shown a relation between the Volume Energy Density (VED), and the final part porosity content, and the strategy then consists in keeping about the same VED from one material to another [14]. The volume energy density is given by:

$$\text{VED} = \frac{\alpha \cdot P}{V \cdot h \cdot L} \tag{1}$$

Where α is the material absorptivity, P the laser power (W), V the laser speed (m/s), h the hatching distance (m), and L the layer thickness (m).

---

* Corresponding author.
E-mail address: hossein.ghasemitabasi@epfl.ch (H. Ghasemi-Tabasi).

However, the VED does not consider all essential quantities, and it is well known that different sets of parameters in Equation (1) may lead to the same VED but different melt pool depths [14], which in turn lead to different part qualities. In other words, there are not enough material related parameters in the VED equation, such that this quantity could be used for translation rules [15].

An alternative to the VED criterion is the construction of process maps based on material and laser process parameters. There are several studies describing the correlations of the melt pool geometry with laser parameters and material properties [16–22]. Ion et al. [23] have applied analytical heat flow parameters in order to develop laser processing diagrams through dimensionless numbers which predict the heating, melting, and evaporation zones for different types of laser and material. The reported tables and diagrams are useful to quantify regimes in different laser processes such as welding, heating, cutting, and cladding. The keyhole formation threshold has been used in several studies as a fundamental model to find the optimum conditions [24–30]. Hann et al. [27] plotted dimensionless graphs to find the transition zone between the conduction mode and the keyhole mode, considering an energy balance between the input and the dissipated energy - which introduced the so-called normalized enthalpy - and comparing it to a normalized melt pool depth. Equations (2) and (3) express the normalized enthalpy $\Delta\bar{H}$, and the normalized melt pool depth $\bar{d}$:

$$\Delta\bar{H} = \frac{\Delta H}{\Delta h} = \frac{\alpha P}{\rho(\ C\Delta T + L_m)\sqrt{\pi\omega^3 VD}} \tag{2}$$

$$\bar{d} = \frac{d}{\omega} \tag{3}$$

Where α is the absorptivity of the bulk material, P is the laser power (W), ρ the density $(\frac{kg}{m^3})$, C the specific heat $(\frac{J}{kg.K})$, ΔT the difference between the melting and initial temperature (K), L_m the latent heat of melting $(\frac{kJ}{kg})$, ω the laser spot radius (m), V the laser speed $(\frac{m}{s})$, D the thermal diffusivity $(\frac{m^2}{s})$, and d the melt pool depth (m). A master curve valid for different materials has been found by plotting the normalized melt pool depth as a function of the normalized enthalpy $\bar{d}$ ($\Delta\bar{H}$). Going to high values of the normalized enthalpy results in keyhole formation, and increases the slope of the $\bar{d}$ ($\Delta\bar{H}$) function [27]. In welding processes, an appropriate process parameters optimization is required to set a balance between different forces inside the melt pool such as to have a stable keyhole [31]. However, high energy densities lead to high evaporation on the melt surface. As a result, a complex liquid flow develops in which instability and collision of the keyhole walls may result in keyhole porosities [32]. Therefore, even though the keyhole mode is frequently helpful for welding to deliver deep penetration and thin bead welds, it is not recommended in AM because of the risk for porosity formation. The conduction mode [33,34] is preferred instead, i.e. the one at lower normalized enthalpy values, where keyholes do not form yet. On the other hand, insufficient heat input during laser processing leads to incomplete melting of the powders and the so-called lack of fusion porosities, which must clearly be avoided. Optimal conditions therefore lie in a transition zone between keyhole and conduction modes: this is where the formation of porosities is expected to be the lowest. Experimental welding data for different materials are in a good agreement with this model, and they all align well with the master curve when varying the process parameters [27].

The above model has been used for additive manufacturing in different studies. King et al. [30] combined the laser process parameters into a graph, based on normalized enthalpy and normalized melt pool depth. The results suggest that the model is useful to identify close to optimum process windows; however, a much higher normalized enthalpy was obtained at the transition zone between conduction and keyhole modes, compared to welding. Scipioni Bertoli et al. [14] did not observe a sharp transition between conduction and keyhole modes,

and their normalized enthalpy at the transition point was also different from the study by King et al. [30]. Alternate versions of the normalized enthalpy expression have been proposed, e.g. by adding dimensionless parameters to characterize the melt pool [35,36] or heat conduction [37] during the SLM process. M. Thomas et al. [38] extended the approach devised by Ion et al. [23] to plot dimensionless graphs based on additive manufacturing process parameters and their model provides useful information for predicting the final microstructure of AM parts; however, it does not provide information concerning the transition zone between different melt pool modes (conduction, keyhole). L. Johnson et al. [39] used characteristic length scales of the melt pool as a printability metric for the SLM process. In their numerical calculation they consider phase transformation between solid, liquid and vapor, neglecting the powder properties, and define artificially high absorptivity and conductivity for the vapor phase. The reported maps provide useful information for different melt pool modes based on laser power and scanning speed; however like in [38], the model fails to clearly capture a transition zone between melt pool modes for different materials.

SLM shares some characteristics with laser welding. However, in the SLM process, the laser interacts with powders which have completely different responses from bulk solid materials in welding. Laser/powder interaction is also a function of the powder size distribution and layer thickness. In processes such as laser cutting, drilling, and welding, when a high power laser irradiates the surface of the material, a part of the beam energy is transferred to the piece by heat conduction. The surface can also melt and even vaporize [40]. When dealing with powders, multiple scattering, and powder geometry effects play a major role in determining the effective optical properties [41]. These aspects have been studied both empirically and by numerical simulation. To simplify the model of light absorption in the powder, in earlier studies, the powder is assumed to be a homogeneous continuum body [42,43]. In their theoretical study, Boley et al. [41] considered the powder bed as randomly distributed particles. Using the ray-tracing method, these authors found that the powder absorption was much larger than the value measured on a flat metal surface, due to multiple light scattering. A real powder bed is made of particles of variable sizes and which are not densely packed, which also influences the absorption [44,45]. The numerical computation reveals that a flat metallic surface or an isolated sphere has a reduced absorptivity compared to powder particles. Multiple reflections inside the powder bed give an effective absorption coefficient which can also be higher than that of the liquid surface [43]. Trapp et al. [46] measured the absorption value for 316 L stainless steel powder, and found that higher ratios of the beam size to the particles size increase the chance for multiple reflections and lead to higher absorptivity.

The experimental evaluation of absorption through temperature measurements is not easy since absorptivity depends on different factors such as laser intensity, angle of incidence, wavelength, temperature, surface chemistry (oxidation), surface roughness, and contamination. As an example, for gold, various absorption models have been considered [47,48]. Gold in the solid-state is known to be very reflective in nature. While other metals like iron, palladium, aluminum, and platinum show a relatively lower reflectivity of 60-70% at the infrared wavelength, copper, silver and gold show almost total reflectivity [49]. Therefore, the surface reflects most of the incident laser energy, and melting these metals by laser is difficult despite their low melting point. However, when using powders, the finite penetration depth of light inside the powder bed significantly increases the absorption compared to the bulk solid state [13,41].

The selective laser melting of tin bronze (CuSn10) powder has been studied in previous studies[50,51]. The first step of this work is to investigate optimum SLM processing conditions for bronze (CuSn8), i.e. those leading to the lowest porosity content. A second step then consists in transferring SLM parameterization results from CuSn8 to red gold and 316 L steel, using an appropriate translation rule. In previous

studies mentioned earlier, authors considered different states of the material for the absorptivity values, i.e. bulk surface ([14,30,35,37,38,52,53], liquid surface [36], and vapor state [39]). In our study, one important ingredient of the translation rule is the *powder absorptivity*, which takes into account the chemical composition, surface roughness, powder morphology, and size distribution [54]. For one specific material, most of the thermophysical properties of the powder particles mainly depend on their shape and size distributions, and on their spatial arrangement. Their temperature evolution is actually very small compared to their variation between powder, bulk solid and liquid state values; this means that room temperature measurements are meaningful even if processing also operates at higher temperatures. For instance, the powder thermal conductivity variation between room temperature and the sintering temperature with temperature is more than 100 times lower than the change from the powder to the bulk solid and the liquid state [55–57]. In the same way, the powder absorptivity evolution over the same temperature interval is negligible compared to the difference associated to the transformation into bulk solid or liquid state [58,59].

The proposed translation rule is finally validated by SLM experiments on red gold and 316 L steel, and justified through finite element simulations using different values of absorptivity for the liquid, bulk solid and powders, while considering a finite optical penetration depth of the laser in the powder bed. The optimal condition acquired from the model is defined based on the density and porosity content of the samples. The generality of the approach is verified by considering a different laser spot size when printing 316 L steel samples.

2. Experimental

2.1. Manufacturing process

Commercially gas-atomized bronze CuSn8 (92 wt.% Cu, 8 wt.% Sn) and 18-carat red gold (75 wt.% Au, 20.5 wt.% Cu, 4.5 wt.% Ag) powders provided by Heraeus Group were used in this study. 316 L steel samples were printed with gas-atomized powder (12 wt.% Ni, 17 wt.% Cr, 2.5 wt.% Mo, 2.3 wt.% Si, 1.0 wt.% Mn, 0.03 wt.% C) provided by Oerlikon. The received powder particles had a spherical shape with some small porosity and very fine rare satellite particles (Fig. 1). The powder particle size distributions and their relative densities are listed in Table 1. The relative density of the powder bed was measured using the Powder Tester HOSOKAWA MICRON CORPORATION machine (supplementary section S1).

SLM experiments used an in-house machine (Fig. 2), intended for research activities [60], and designed for operating with only a few dozen grams of powder. It is equipped with a 500 W fiber SPI laser, with a wavelength of 1070 nm and with the possibility to use two different laser spot sizes (65 μm and 85 μm). Optimization of SLM parameters was done under a nitrogen atmosphere, with oxygen content controlled below 200 ppm throughout the process.
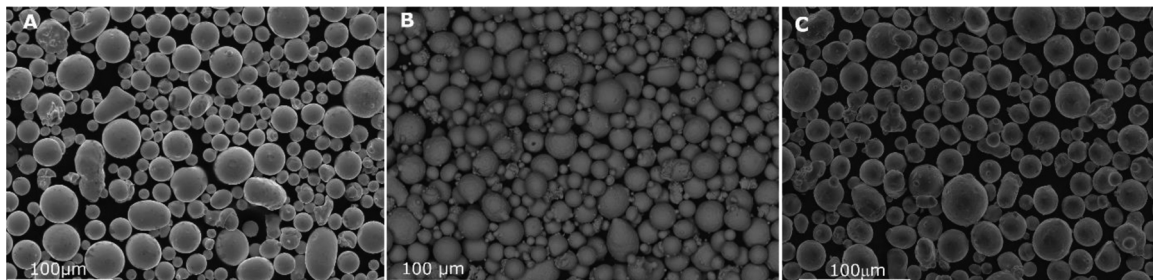
Table 1
Bronze, red-gold, and 316 L powders particles details.

	D10 (μm)	D50 (μm)	D90 (μm)	Relative density %
Bronze	20.11	31.11	44.25	59.7
Red-gold	13.77	26.63	40.84	54.8
316 L	18.24	30.04	45.65	55.3

2.2. Optical properties measurements

Powder and bulk material absorptivities of the different materials were measured for wavelengths from 900 to 1200 nm with a Perkin Elmer Lambda900 spectrophotometer. For the powder particles, the measurements were done in both transmission and reflection modes. Fig. 3 indicates different phenomena occurring during the optical measurement of the powder layer with the spectrophotometer. The measured layer thickness of the powder is around 40 μm, which corresponds well to the SLM layer thickness in our experiments. The measured reflectivity and transmitivity of the powder bed are named R and T, respectively.

The amount of light (per unit area of the top surface) penetrating inside the powder layer is equal to:

$$I_0 - I_r = (1 - R) I_0 = \alpha_p I_0 \tag{4}$$

Where I_0 is the intensity of the light on the top surface, I_r is the intensity of the reflected light, and α_p is the *total powder absorptivity*. A part of the penetrating light in the powder bed is absorbed within the powder layer (I_{abs}) and the remaining part is transmitted at the other side of the layer (I_t). We can then define the *powder layer absorptivity* (α_{p_layer}) by:

$$I_{abs} = I_0 - I_r - I_t = (1 - R - T)I_0 = \boldsymbol{\alpha_{p\_layer}} I_0 \tag{5}$$

One could object that, during the SLM process, the fraction of light reaching the bottom side of the layer will be either absorbed or back-reflected by the substrate or the previously solidified layers. However, due to the surface roughness induced by SLM processing which reduces reflectivity, and the fact that back-reflections go in all directions [61,62], we assume that the amount of light really contributing to the local heating of the powder layer under the laser spot is closer to α_{p_layer} than α_p. Such an assumption would require proper simulations at the right scale to be validated [63,64].

The optical penetration depth in the powder bed is calculated from the spectrophotometer measurements. In a homogeneous medium, the radiation intensity perpendicular to the medium surface decays according to the Beer-Lambert law [49]. The intensity of the transmitted radiation (I_t) at a distance L from the material layer top surface (Fig. 3) is then:

$$I_t = I_0 \, T = \alpha_p I_0 e^{-\frac{L}{\delta}} \tag{6}$$

Where L is the layer thickness, and δ the optical penetration depth defined as the depth at which the beam intensity falls to 1/e of the top surface value. In other words, $\alpha_p I_0$ indicates the amount of light entering the powder layer and $e^{-\frac{L}{\delta}}$ the intensity decay at distance L from
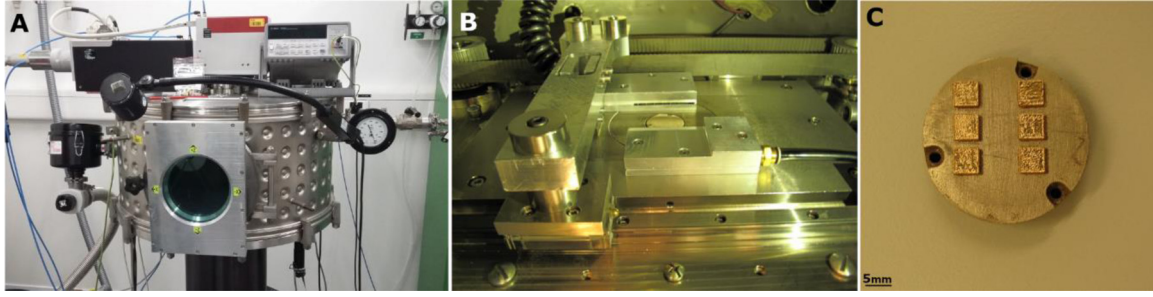

Fig. 1. SEM images of the A) 18-carat red gold, B) bronze, and C) 316 L gas atomized powders morphologies.

Fig. 2. A) In-house SLM machine, B) printing plate, powder deposition, and gas flow system, and C) example of printed bronze samples.
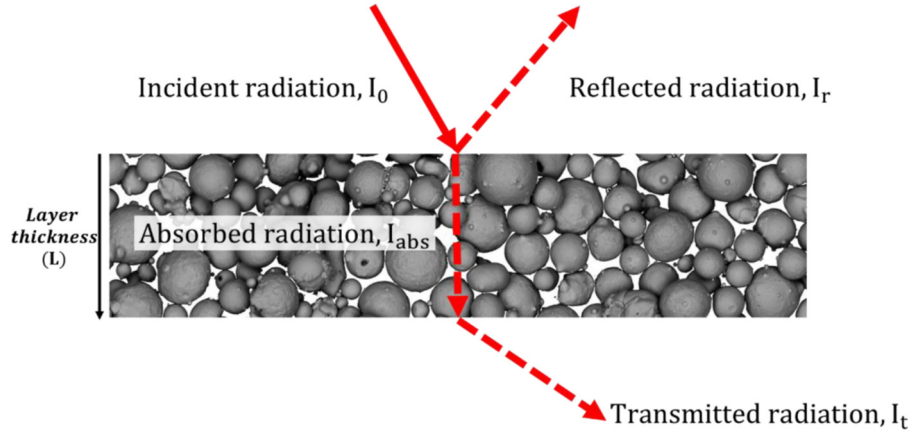

Fig. 3. Schematic view of beam reflection, transmission, and absorption inside the powder bed during the optical properties measurement with the spectro-photometer.

the top surface. With the same approach as Equation (6), the amount of absorbed intensity inside the powder bed (I_{abs}) will be:

$$I_{abs} = \alpha_p I_0 (1 - e^{-\frac{L}{\delta}}) \tag{7}$$

Which then defines the relation between α_p and α_{p_layer} :

$$\alpha_p = \frac{I_{abs}}{I_0(1 - e^{-\frac{L}{\delta}})} = \frac{\alpha_{p\_layer}}{(1 - e^{-\frac{L}{\delta}})} \tag{8}$$

For red gold powders, the effect of a heat treatment was also considered such as to quantify the change of absorptivity related to oxidation of the powder particles surface [65]. The oxide formation is in fact used in several studies to increase absorptivity and reduce the porosity content in the final part [12,66]. In this study, the chosen heat treatment was four hours at 200 °C.

2.3. Samples characterization

2D optical microscopy analysis was conducted using a Leica DM6000 M microscope to evaluate the distribution of pores within the SLM samples, and measure the melt pool geometries. The samples were ground using a SiC paper up to 2500 grit size and then polished with a suspension of alumina particles until 0.25 μm. For each sample, three different parallel sections (5 × 5 mm) were evaluated at a magnification of 10 × . The stitching of the figures was done using the software tool of the Leica microscope. To characterize the melt pools, bronze samples were etched with a H_2O + 25 ml NH_3 + 5 ml H_2O_2 solution, and red gold samples with a cyanide-based solution. Diluted Aqua regia solution (75 ml HCl + 25 ml HNO_3 + 100 ml H_2O) was used to characterize the melt pool of the 316 L printed samples. The porosity distribution was characterized by 2D image analysis of the three metallographic cross-sections, using the ImageJ software with a plugin [30], and the values are reported with a fractional uncertainty of maximum 0.08%.

2.4. Finite element simulations

A dedicated finite element simulation software has been developed for the modeling of the SLM process [67]. In this code, the powder bed is considered as a homogeneous medium, which has effective properties (absorptivity, thermal conductivity, optical penetration depth, density).

The mesh in the parallelepiped computation domain Ω (the powder bed and its surrounding) is illustrated in Fig. 4. Five different zones can be distinguished based on the (isotropic) mesh size; mesh adaptation follows the laser scanning direction such as to keep the laser spot at the center of the most refined zone. The mesh extends in the z-direction by extrusion of the 2D mesh shown in Fig. 4. The elements in the coarse and fine mesh are tetrahedra and orthogonal prisms, respectively [68]. The elements sizes are determined based on the heat source spatial distribution and considering the needed accuracy for the computation of thermal conduction within the powder and at the interface between the powder and the bulk solid or liquid.

Different optical properties are considered for the solid, liquid and powder states. The light penetration inside the powder bed is defined by Equation (6). Generally, for bulk metals, the light penetration depth δ is very small (in the order of tens of nanometers) [69]; therefore, a surface heat source is used when dealing with the liquid or the bulk solid. However, for powders particles with sizes in the range 10-40 μm, the penetration depth δ is of the order of several powder particle diameters [70]. Therefore, in the SLM process for which the powder bed thickness is lower than a hundred microns, the effect of the penetration depth in energy deposition is certainly not negligible [43]. For this reason, the laser heat source is modeled, in the powder bed, as a *volumetric* source.

In the finite element code, the temperature T and the enthalpy per unit mass u result from the heat transfer in Ω. The evolution of u follows from the heat diffusion equation, with appropriate boundary and initial conditions (Eqs. (9)–(11)):
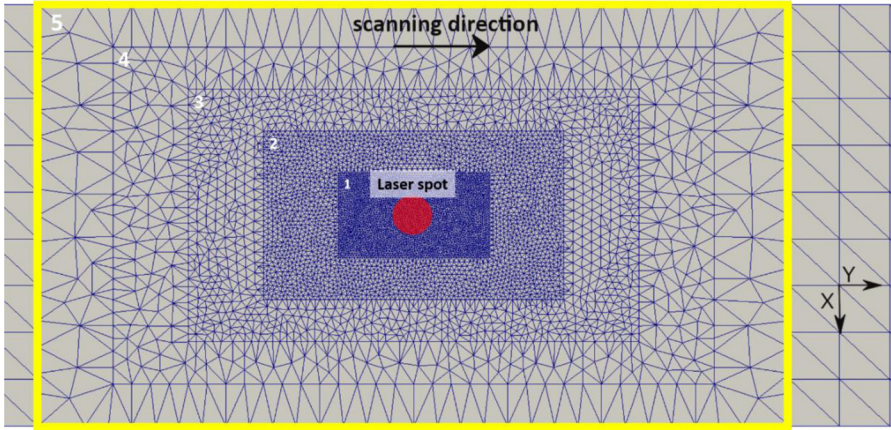
Fig. 4. Top view of the non-conformal mesh used in finite element simulations of the SLM process. Five different zones are defined inside the moving mesh (indicated by the yellow box), which follows the laser scanning during the simulation. The laser scanning plane is the (x, y) plane.. The maximum areas (mm^2) of the elements in the (x, y) plane are, 0.00000625, 0.000025, 0.0001, 0.0004, and 0.0016, for zones 1, 2, 3, 4, and 5, respectively.

$$\rho \frac{\partial u}{\partial t} - \nabla(K\nabla T) = F, \text{ in } \Omega \tag{9}$$

$$K\frac{\partial T}{\partial n} = \kappa(T_0 - T) + f, \text{ on } \partial\Omega \tag{10}$$

$$u = u_0, \text{ in } \Omega, \text{ for } t = 0 \tag{11}$$

Where K is the effective thermal conductivity, ρ the density, κ the thermal exchange coefficient between the domain and the environment (at a temperature T_0), F a volumetric heat source and f a surface heat source. $\frac{\partial T}{\partial n}$ is the normal outward derivative of the temperature on the surface boundary of the computational domain $\partial\Omega$. The temperature T is linked to the enthalpy per unit mass u by an algebraic equation:

$$T = \beta(u) \tag{12}$$

where β is a non-decreasing real-valued function of the real variable u. In our program, the function β is constructed according to the information on the heat capacity of the material and on the latent heats of its phase changes[71].

All material properties used in the numerical simulations are summarized in Tables 2 and 3. For all three materials, evolutions of properties with temperature are taken from the references listed in Table 3. For bronze and red gold alloy, due to a lack of experimental thermophysical property data, fewer data points are available, compared to 316 L. The computations considered the stabilized melt pool size (i.e. in quasi-steady state). The thermal conductivity of the powder particles is set two orders of magnitude smaller than that of the bulk solid state, due to the air gap between particles.

3. Results and discussions

3.1. Optimization of SLM parameters

Bronze samples (5 × 5 × 3 mm) with different SLM parameters were printed. The analysis of samples is conducted to evaluate the distribution of pores within cross-sections. The selected optimal parameters, for a laser spot diameter of 85 μm, were a power of 250 W, a scanning speed of 200 mm/s, a hatching distance of 150 μm and a layer

Table 2
Optical properties of bronze, red gold, heat-treated red gold and 316 L steel in the different states (solid (s), liquid (l), and powder (p)), at 1070 nm wavelength.

	α_s%	α_l%	α_{p_layer}%	δ (μm)
Bronze	11.05	11	44.27	27.30
Red Gold	10.8	10	20.82 (27.91)[a]	53.82(49.98)[a]
316 L	29.05	20[80]	52.59	25.81

[a] Thermally treated red gold powder.

thickness of 40 μm, leading to a relative density of 99.87%. Fig. 5-A illustrates a cross-section of one printed bronze sample with optimized parameters. Using the exact same parameters for the red gold sample gave a highly porous material (Fig. 5-B, 93% relative density), which clearly indicates the need for a translation rule.

3.2. Derivation of a translation rule from one material to another

Equation (2) is now rewritten with effective parameters taking into account the different states of the material involved in SLM (powder, liquid and bulk). $\bar{\Delta H}^j$ is the normalized enthalpy of the material j (in this work: bronze(B), red-gold(G), or 316 L steel(S)) as a function of the processing conditions. Equations (13) and (14) express the normalized enthalpy $\bar{\Delta H}^j$, and the normalized melt pool depth $\bar{d}$:

$$\bar{\Delta H}^j = <\alpha>^j \cdot M^j \cdot \frac{P}{\sqrt{\omega^3 V}}$$

$$\text{with } M^j = \frac{1}{\rho(C\Delta T + L_m)\sqrt{\pi <D>}} \tag{13}$$

$$\bar{d} = \frac{d}{\omega} \tag{14}$$

Where $<\alpha>^j$ is the effective absorptivity value of material j during the SLM process, and M^j contains all the other properties of the material as defined in section 1. <D> is the effective diffusivity of the material. During the SLM process operating in the conduction mode, the laser interacts with both the powder and liquid phases and therefore, considering Equation (8), the incident power P_0 is distributed between the liquid and powder phases according to:

$$<\alpha>^j \cdot P_0 = \alpha_p^j P_p + \alpha_l^j P_l = \frac{\alpha_{p\_layer}^j}{(1 - e^{-\left(\frac{l^j}{\delta^j}\right)})} \cdot P_p + \alpha_l^j \cdot P_l \tag{15}$$

Where α_p^j and α_l^j are the powder and liquid absorptivities of material j, respectively, and P_p and P_l are the amount of incident power interacting with powder and liquid phases, respectively. From Equation (15), the effective absorptivity value is then:

$$<\alpha>^j = \frac{\alpha_{p\_layer}^j \cdot P_p}{(1 - e^{-\left(\frac{l^j}{\delta^j}\right)}) \cdot P_0} + \frac{\alpha_l^j P_l}{P_0} \tag{16}$$

If we define $\frac{P_p}{P_0}$ as the fraction f_p of the incident laser power interacting with the powder particles, and $\frac{P_l}{P_0}$ as the fraction $f_l = 1 - f_p$ interacting with the liquid phase, we have:

Table 3
Physical properties of solid (room temperature) /liquid (melting point) bronze, red gold, and 316 L steel.

|	Density (kg/m³)	Thermal diffusivity (m²/s)	Specific heat (J/kg.K)	Melting/Boiling point point (K)	Latent heat of fusion/evaporation (kJ/kg)
Bronze solid	8800[81]	1.8×10^{-5}[82]	371[83]	1163[83]	180[84]
Bronze Liquid	8800[a]	1.8×10^{-5} [a]	371[a]	2573[85]	1800
Red gold solid	15100[86]	2.1×10^{-5}	193[87]	1183[86]	62
Red gold liquid	15100[a]	2.1×10^{-5} [a]	193[a]	3370[85]	620
316 L solid	7900[88]	3.5×10^{-6}[88]	490[88]	1640[88]	260[88]
316 L liquid	6920[88]	3.84×10^{-6}[88]	770[88]	3090[88]	7450[89]

[a] Same value for solid and liquid.
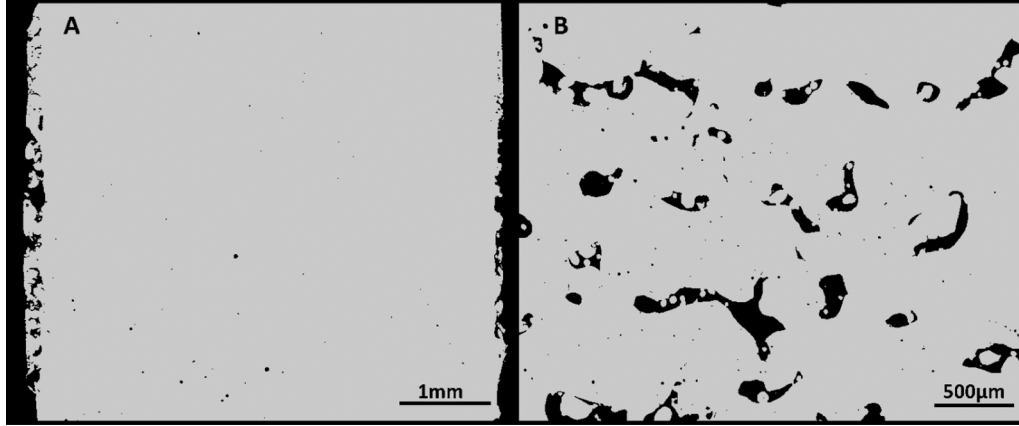
Fig. 5. Optical micrographs (X-Y plane) of the A) optimized bronze sample, and B) manufactured red gold sample with the parameters used to obtain an optimized bronze sample in figure A).

$$
< \alpha >^j = \frac{\alpha^j_{P\_layer}}{\left(1 - e^{-\left(\frac{L^j}{\delta^j}\right)}\right)} . f_p + \alpha^j_l . f_l = \alpha^j_{p\_layer} \left[\left(\frac{1}{1 - e^{-\left(\frac{L^j}{\delta^j}\right)}} \right) . f_p \right.
$$

$$
\left. + \left(\frac{\alpha^j_l}{\alpha^j_{p\_layer}} \right) . f_l \right] = G^j . \boldsymbol{\alpha^j_{p\_layer}}
$$

(17)

Where G^j is a material-dependent value.

Table 2 summarizes absorptivity values for different materials and different physical states. The absorptivity values were obtained from spectrophotometer measurements on a powder layer (α_{p_layer}, see Fig. 3) or a polished bulk solid (α_s). All measurements were done at room temperature, as discussed in section 1. In the infrared range, the red gold powder absorptivity increased after heat treatment by about 8%; however, it was still significantly lower than the bronze value. The reported optical properties of the liquid phases in Table 2 are taken from literature considering pure gold and pure copper [72,73] (approximating red gold and bronze, respectively). All other material parameters are given in Table 3. Due to the lack of available thermophysical properties for liquid bronze and red gold, a few quantities were taken identical for the solid and the liquid.

In Table 2, liquid absorptivities are all significantly lower than the corresponding powder absorptivities, which gives an increased weight of the powder over the liquid when computing normalized enthalpies. Equation (13) describes the energy balance between the input energy of the laser source and the dissipation of the energy due to thermal losses. The thermal losses are mainly classified in radiation, vaporization and splattering, convection, and conduction losses [74]. From the experimental measurements and theoretical computations, the primary heat dissipation mechanism is conduction through the bulk solid phase [75,76]. Consequently, as a **first approximation (i)** we choose the thermal diffusivity of the solid phase (D_s) in Equation (13), instead of the effective diffusivity $<D>$, to describe the dissipation of the energy.

The input energy can be divided into the light absorbed by the melt pool, the powder bed, and at higher energies, by vapor plumes and plasma produced by the melt pool. In additive manufacturing, laser powers used for melting of the powder layer are in general lower than in welding applications, mainly to prevent porosities created by the keyhole regime. The absorbed laser light in vapor and plasma during low-power laser welding is around 15%, as discussed by R. Miller et.al [77]. In the SLM process, the conduction mode leads to minimal vaporization; thus, the majority of the energy is absorbed by the melt pool and the powder bed. The melt pool lifetime is directly proportional to the process parameters and thermal diffusivity [78,79]. For highly conductive materials such as bronze and gold, it is even shorter than for convention materials. Part of the heat absorbed by the melt pool is transferred to the surrounding material, but very little to the powders, due to their low thermal conductivity. Consequently, the energy used to melt the powder is essentially the one directly absorbed by multiple scattering of the laser beam coming on the powder bed. Since the exact value of $<\alpha>^j$ is not easily measurable as the laser interacts with different material states in unknown proportions, as a **second approximation (ii)**, we consider that in Equation (17), G^j is *material insensitive*, so that only the powder layer component $\alpha^j_{p\_layer}$ of the effective absorptivity is important when comparing different materials.

The combination of approximations (i) and (ii) finally leads to:

$$
\bar{\Delta H}^j \approx \boldsymbol{\alpha^j_{P\_layer}} . M^j . \frac{P}{\sqrt{\omega^3 V}}
$$

$$
\text{with } M^j = \frac{1}{\rho(C\Delta T + L_m)\sqrt{\pi D_s}}
$$

(18)

Both approximations (i) and (ii) will be validated further in this paper by finite element simulations (section 3.4). Fig. 6 is a schematic view of the SLM process and summarizes the assumptions which are considered to derive the translation rule below.

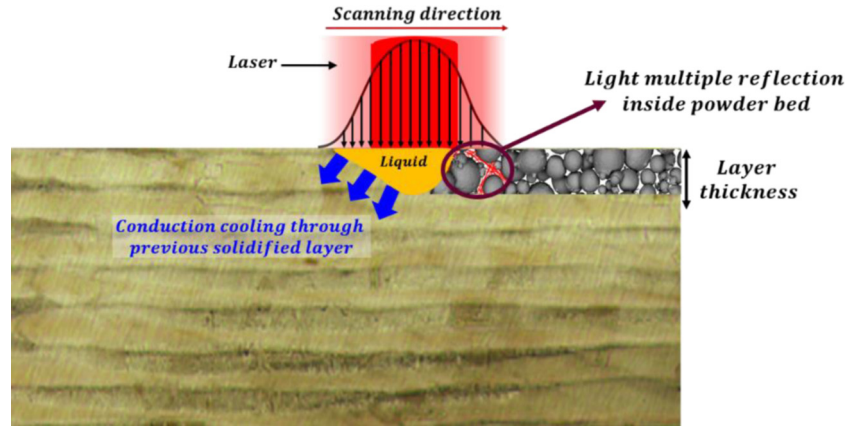The optimal normalized enthalpy value (ΔH^{opt}) in Equation (18),

Fig. 6. Schematic view of the SLM process indicating energy coupling and heat transfer paths considering the different states of the material (solid, liquid, powder).

based on the powder absorptivity values of bronze or any other alloy A, $\alpha^B_{p\_layer}$ and $\alpha^A_{p\_layer}$ respectively, is:

$$\Delta \bar{H}^{opt} \approx \alpha^B_{p\_layer} \cdot M^B \cdot \left(\frac{P}{\sqrt{\omega^3 V}} \right)^{opt}_B$$

$$= \alpha^A_{p\_layer} \cdot M^A \cdot \left(\frac{P}{\sqrt{\omega^3 V}} \right)^{opt}_A \qquad (19)$$

From equation (19), the **translation rule** (20) follows, defining the optimal alloy A processing conditions:

$$\left(\frac{P}{\sqrt{\omega^3 V}} \right)^{opt}_A = \left(\frac{\alpha^B_{p\_layer}}{\alpha^A_{p\_layer}} \right) \cdot \left(\frac{P}{\sqrt{\omega^3 V}} \right)^{opt}_B \cdot \frac{M^B}{M^A} , \qquad (20)$$

where $\left(\frac{P}{\sqrt{\omega^3 V}} \right)^{opt}_B$ and $\left(\frac{P}{\sqrt{\omega^3 V}} \right)^{opt}_A$ represent the optimal SLM laser power and scanning speed for bronze and alloy A, respectively. Differences in laser spot size ω can also be accounted for.

3.3. Applying the translation rule to red gold and 316 L

Normalized melt pool depths have been measured for the different investigated materials. Fig. 7 shows the $\bar{d}(\Delta \bar{H})$ curve of the normalized melt pool vs the normalized enthalpy for bronze samples, considering only the powder layer contribution to $\Delta \bar{H}$ according to (18). Fig. 7 captures well the transition between conduction and keyhole regimes, indicated by a significant change of the curve slope.

Translated parameters for printing red gold and 316 L steel samples are listed in Table 4. They were determined by changing the laser power and speed such as to satisfy Equation (20). Only small adjustments were performed afterwards, leading to the optimum points for red gold and 316 L represented by the green square and orange triangle in Fig. 7. It is underlined that 316 L steel was printed with a different laser spot size ω (65 μm instead of 85 μm), which explains the different hatching distance in Table 4, and also tests the generality of the translation rule. The hatching distance for the 316 L steel sample has been chosen such as to keep about the same ratio between the beam diameter and the hatching distance as the one used for bronze.

The analysis of microstructures confirms the very low porosity content in both red gold and 316 L steel samples (Figs. 8 and 9). These results show major improvements in printing gold alloy samples with a high relative density, compared to previous studies where the authors had to change the alloy composition to print samples with a reasonable density [11]. The porosity content for the thermally treated red gold powder sample is more than for the untreated powder sample, which is attributed to the presence of oxide, known to promote porosity formation, and its stabilization and growth [90].

The optimal normalized enthalpy ($\Delta \bar{H}$), normalized melt pool depth ($\bar{d}$), and relative densities values for bronze, red gold, and 316 L samples are summarized in Fig. 9. Process parameters slightly on the right of the optimal zone would bring closer to the onset of the keyhole mode, and, on the other hand, using parameters on the left side of the optimal point would decrease the melt pool size and increase the porosity content (see supplementary section S2). However, samples printed with process parameters close to the optimal zone always keep high relative densities compared to those with very different $\Delta \bar{H}$ values. This is in fact the interesting feature of the proposed model, as printing samples close to the reported optimal value guarantees low porosity content. The outcome is important not only when dealing with precious powders like gold, but also for any new material, for which the number of trials and errors is reduced.

3.4. Finite element simulations

Finite element simulations of SLM were performed in order to check the validity of the approximations made in the previous section: (i) consider the bulk solid value for the thermal diffusivity in Equation (18), and (ii) only consider the powder layer absorptivity in the translation rule (20).

Fig. 10 shows the FEM simulated and experimental melt pool depth values for printed bronze samples, using the optical and physical parameters given in Tables 2 and 3. In the conduction mode, there is a good agreement with experiments, when considering three phases (powder, bulk solid, and melt) with different values of absorptivity and thermal diffusivity. Using the bulk solid value for the diffusivity (Table 3), the predicted melt pool sizes vary by less than 10%, which reasonably validates the assumption (i) recalled above.

As the fluid flow and the keyhole formation mechanism are not considered in the numerical model, the simulated melt pools depths in the keyhole mode are, as expected, strongly underestimated. However, since the optimal process zone corresponds to much lower normalized enthalpies (conduction mode), such calculations are actually not needed to validate our approximations (i) and (ii), and the resulting translation rule.

Fig. 11 (A-B) indicates the temperature distributions predicted by the finite element simulations applied to bronze and red gold, in steady-state conditions (the liquid phase appears in yellow to red). The selected SLM conditions are the identified optimal ones shown in Fig. 7 and detailed in Table 4. Thermal gradients look similar for both materials. However, the absolute values of temperatures are higher in red gold. Fig. 11 (C-D) represent the laser intensity absorbed by the material and show how it distributes between the powder and the liquid. These results demonstrate a significant direct interaction between the laser source and the powder bed during the manufacturing process, besides the interaction with the melt pool. As described earlier, the
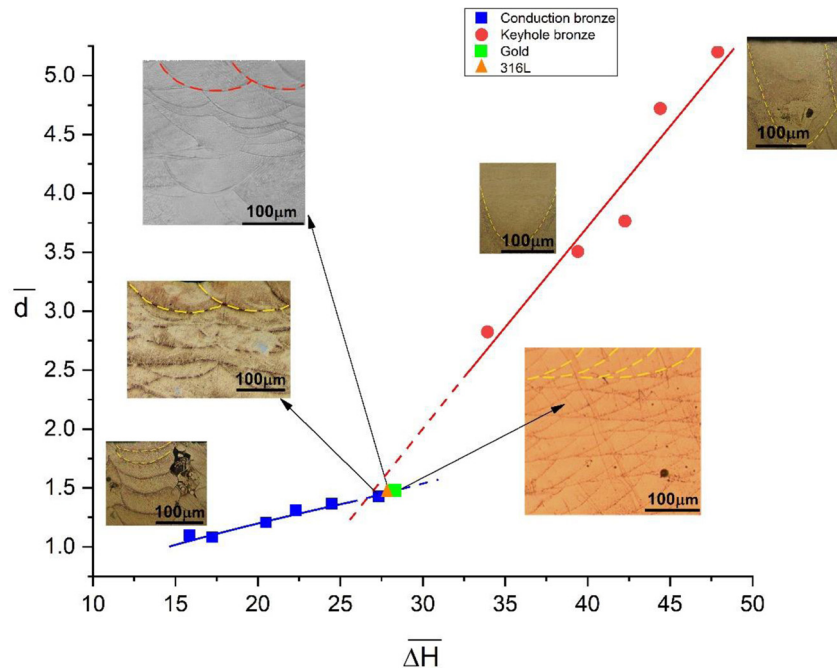
Fig. 7. Normalized enthalpy of the printed bronze samples (Eq. (18)) versus the normalized melt pool depth. In green, the optimal conditions for the red gold sample. In black, the optimal conditions for 316 L steel.

penetration of the light into the depth of the powder bed is implemented in the code such that the heat source term becomes volumetric [89]. This feature is of high importance when defining a layer thickness ensuring metallurgical contact with the previously solidified material. The amount of light absorbed at the front of the melt pool as observed in the simulations influences the thermal interactions strongly, and therefore the melt pool geometry.

The changes in the laser power and scanning speed described in Table 4, using the translation rule, were based on approximations (i) and (ii). Approximation (ii) can be further investigated with the present simulations, looking at the interaction of the laser with both the powder bed and the liquid, and computing their relative contributions to thermal exchanges.

Fig. 12 indicates, in the steady-state, the fraction of the total absorbed power in bronze which goes to the powder bed ($\frac{\alpha_p^B \cdot P_p}{<\alpha>^B \cdot P_0}$), for different normalized enthalpy values, while the complementary part is being absorbed by the liquid. For small values of $\Delta\bar{H}$ (faster scanning speed, lower laser power), the fraction absorbed by the powder is higher, and we conclude that powder absorption dominates the process. However, this regime leads to an increase in porosity content related to lack of fusion. At larger values of $\Delta\bar{H}$, the relative density increases and reaches its maximum at the near keyhole threshold, indicated by the green point in Fig. 12. At this point, almost 26% of the power remains absorbed by the powder bed. Larger values of $\Delta\bar{H}$ lead to keyhole formation which cannot be modelled with the finite element model, as already mentioned, which means that the computed fraction of absorbed power in the liquid is most likely underestimated. Again, this is not an issue in practice, as we are only interested in the conduction

mode regime.

Fig. 13 indicates how the input power is distributed into the melt pool and the powder bed, compared to the beam location. The absorbed power is represented on the left part of the image, and the temperature field is given on the right side (the liquid phase appears in yellow to red). The beam spot size is superimposed (yellow circle), considering a spot size definition at $1/e^2$ of the maximum intensity. With this definition, the laser beam mainly interacts with the liquid phase, however a small part of the beam and the tails of the Gaussian distribution do cover the powder bed as well, and this is particularly clear ahead of the melt pool, where the absorbed power is increased due to the higher absorptivity and penetration depth of the powder. These results are in agreement with [36,46] where authors both numerically and experimentally studied the total absorptivity evolution during the SLM process. Their results indicate that the total absorptivity is dominated by the powder bed at the beginning of the melting process, still allowing multiple reflections to occur. Melting and wetting of the powder material also result in a relatively flat surface and reduce the total absorptivity. Moreover, from [91], it is also found that in the conduction mode, multiple reflections inside the powder bed occur in the front head of the melt pool. We can therefore conclude that powders essentially heat ahead of the melt pool due to light being directly absorbed by the powder particles.

To understand better the applicability of the translation rule, the ratio $G^j = \frac{\langle\alpha\rangle^j}{\alpha_{p\_layer}^j}$ is plotted in Fig. 14 as a function of the normalized enthalpy, using the FEM calculated values of $\langle\alpha\rangle^j$.

At very small values of $\Delta\bar{H}$, G^j tends to 1 since there is not enough input energy to form a liquid phase, i.e. the laser only interacts with

Table 4
Bronze optimized parameters and translated ones for two different red gold powders and 316 L steel.

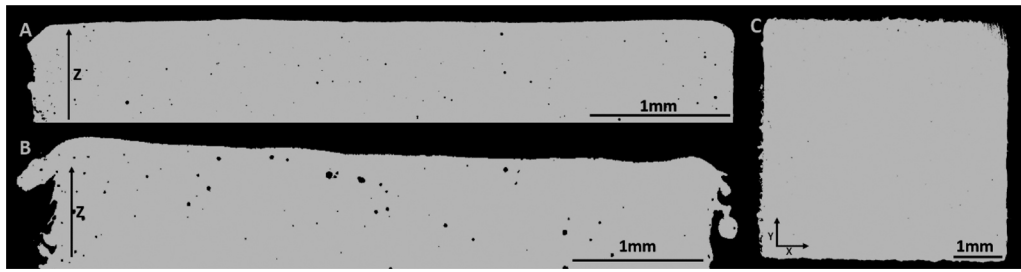|	Power(W)	Speed(mm/s)	Hatching distance(μm)	Layer thickness(μm)	$\omega(\mathbf{\mu m})$
Bronze	250	200	150	40	42.5
Untreated red gold	500	188	150	40	42.5
Thermally treated red gold	375	200	150	40	42.5
316 L	155	490	110	40	32.5

Fig. 8. Micrographs of the printed red gold samples and 316 L steel with translated parameters from bronze, A) untreated red gold, B) thermally treated red gold, and C) 316 L steel.

powder particles. For increasing values of $\Delta\bar{H}$, the powder contribution decreases. The G^j variation is systematically dominated by the higher reflectivity of the liquid phase (regardless of the material) in comparison to that of the powder bed.

We can notice that the value of G^j for different materials at different $\Delta\bar{H}$ values are quite similar, so that we can consider this value to be indeed *material insensitive*, especially when approaching the transition between the conduction mode and the keyhole regime. This can be summarized by the following equation (which is only valid for the conduction mode):

$$\left(\frac{\alpha_{p\_layer}^B}{\alpha_{p\_layer}^A}\right) \cong \left(\frac{\langle\alpha\rangle^B}{\langle\alpha\rangle^A}\right) \tag{21}$$

These results clearly validate the second approximation (ii) in the translation rule, i.e. the material insensitivity of the G^j value in Equation (17).

For the three materials covered in this study, G^j values at the optimal condition vary in the range 0.30-0.38. Considering typical layer thicknesses values used in the SLM process [92], optical penetration depths in the powder bed, and different values for liquid and powder absorptivities, it is possible to identify, from Equation (17), ranges of values for $\frac{L}{\delta}$ and $\frac{\alpha_l^j}{\alpha_p^j}$ which result in similar G^j values :

$$\left.\begin{array}{l} 0.1 < \dfrac{L}{\delta} < 3.5 \\[2mm] 0.1 < \dfrac{\alpha_l^j}{\alpha_p^j} < 0.4 \end{array}\right\} \rightarrow 0.30 < G^j < 0.38 \tag{22}$$
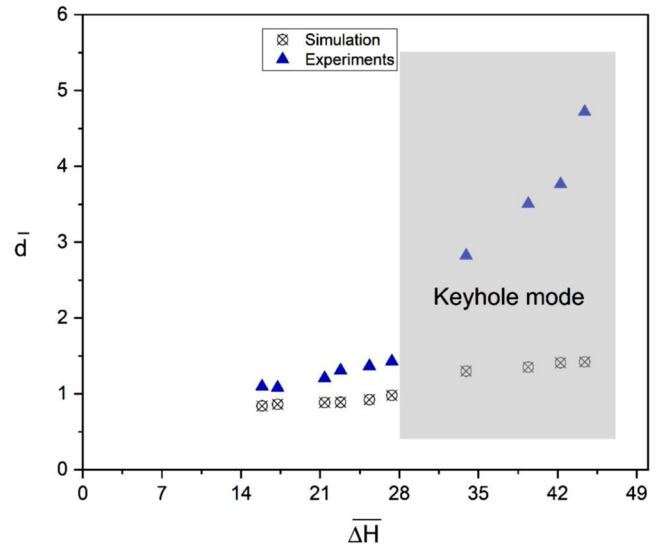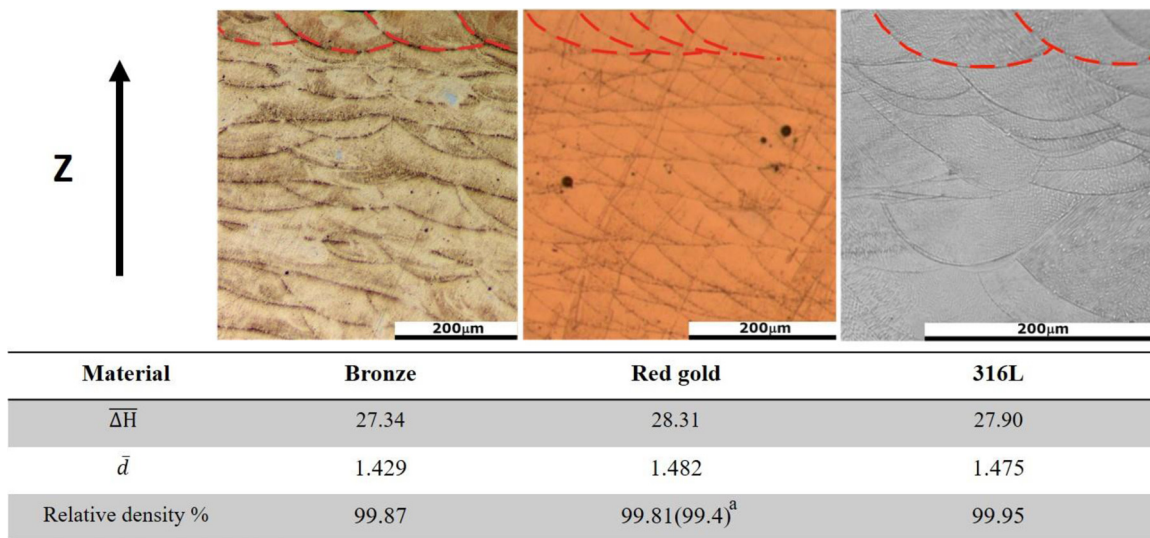

Fig. 10. Experimental and simulated melt pool depth values for printed bronze samples.

Any material for which relations (22) are satisfied should, in principle, be suitable for optimizing the SLM conditions through the translation rule. The supplementary section S3 gives additional details concerning the optical properties measured for powder and bulk materials investigated in this work.

Material	Bronze	Red gold	316L
$\overline{\Delta H}$	27.34	28.31	27.90
$\bar{d}$	1.429	1.482	1.475
Relative density %	99.87	99.81(99.4)[a]	99.95

[a]. Thermally treated red gold powder

Fig. 9. a) Micrographs showing the melt pool geometry (Note: the vertical arrow indicates the build-up direction) b) Normalized enthalpy, normalized melt pool values, and relative densities of bronze, red gold, and 316 L samples printed using the translation rule.
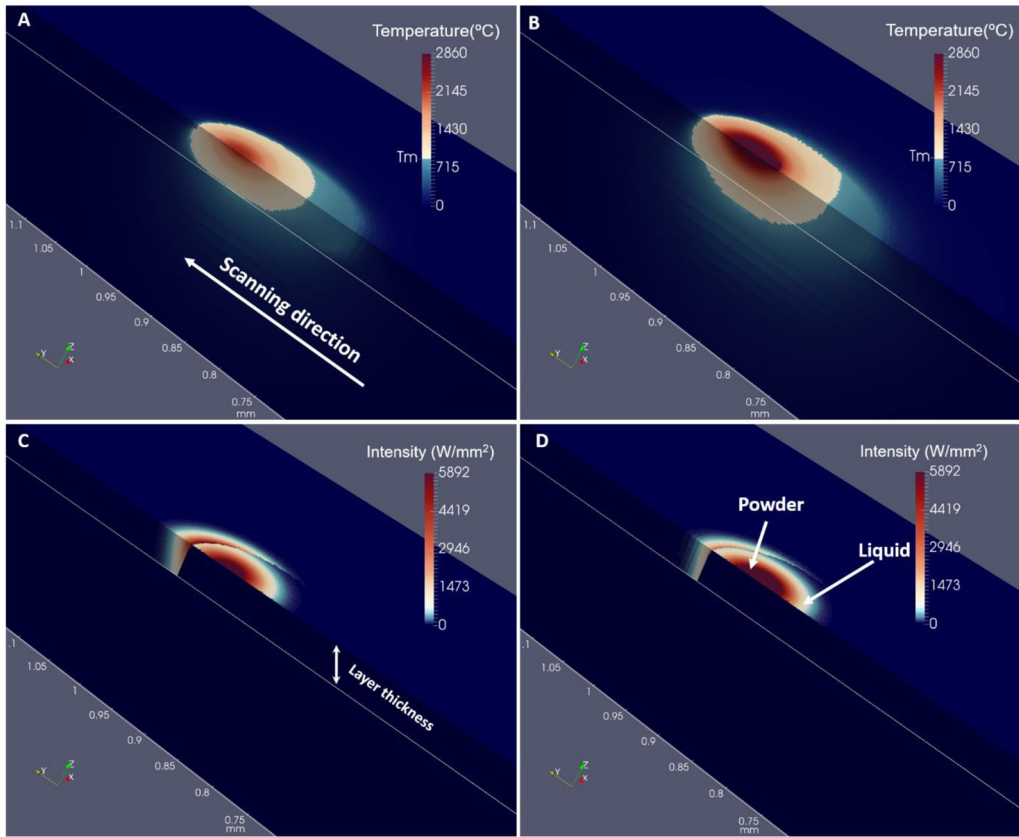
Fig. 11. Simulation results of the SLM process for bronze and red gold, in optimal conditions. (A-B) temperature field in bronze and red gold (˚C), respectively, (C-D) laser absorbed intensity (W/mm^2) for bronze and red gold, respectively.
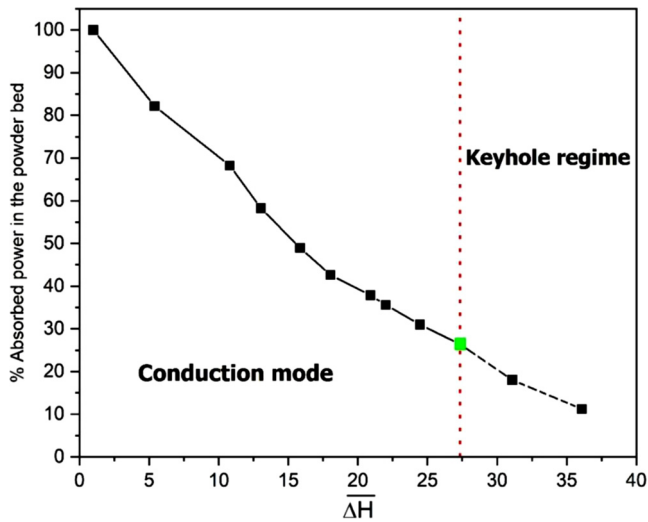

Fig. 12. Simulated fraction of the total absorbed power in bronze going to the powder bed, after melt pool stabilization. The optimal processing condition (highest relative density) is highlighted in green. The dashed line corresponds to the keyhole regime, whose mechanism is not modeled, and is therefore only an extrapolation.

In summary, it is here demonstrated that the proposed translation rule can predict optimal process parameters for a large range of materials, using a simple powder layer absorptivity measurement performed at room temperature.

The validity of the translation rule is related to the importance of the powder absorptivity ahead of the melt pool, when operating in the conduction mode. Light penetrates deeply into the powder bed and largely influences the overall thermal behavior of the melt pool. The story completely changes when entering the keyhole regime, as the complex melt pool geometry then starts absorbing most of the incident light and consequently removes the effect of the powder absorptivity [93,94].

4. Summary

In this study, a model has been developed to translate optimized SLM process parameters from one material to another, based on one simple measurement of powder absorptivity at room temperature. It has been applied to bronze, red gold and 316 L stainless steel, and validated experimentally. Finite element simulations considering variable absorptivities and thermal properties for different materials and states justify the translation rule and its generality. The following conclusions can be drawn:

(1) SLM process parameters for bronze have been optimized to achieve a high relative density of 99.87 %. The optimized parameters correspond to the transition zone between conduction and keyhole modes, and are conveniently identified by plotting the normalized melt pool depth versus the normalized enthalpy of the material.

(2) The bronze optimized parameters have been translated to red gold and 316 L steel, based on the difference in materials thermal properties and measured powder absorptivity. 2D image analysis of metallographic cross-sections show samples with excellent quality, and a porosity content equivalent to the bronze one. To the authors' knowledge, the amount of porosity results is the highest relative density (99.81%) achieved for an additively manufactured 18-carat gold alloy, when using an infrared laser.

(3) The temperature field and the laser power absorbed by the material during the SLM process have been numerically calculated using an in house finite element code. The simulation results indicate
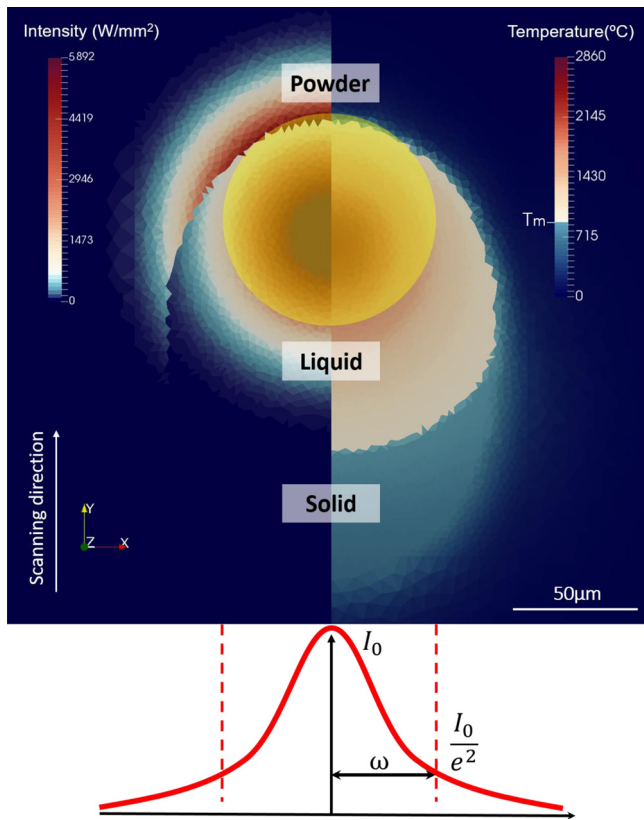
Fig. 13. Simulated temperature distribution (right) and absorbed power intensity in powder bed and melt pool (W/mm^2) (left) in bronze, during the SLM process. The laser beam size ($1/e^2$) is represented by the yellow circle. A Gaussian profile schematically indicates the beam intensity distribution corresponding to the laser beam size.
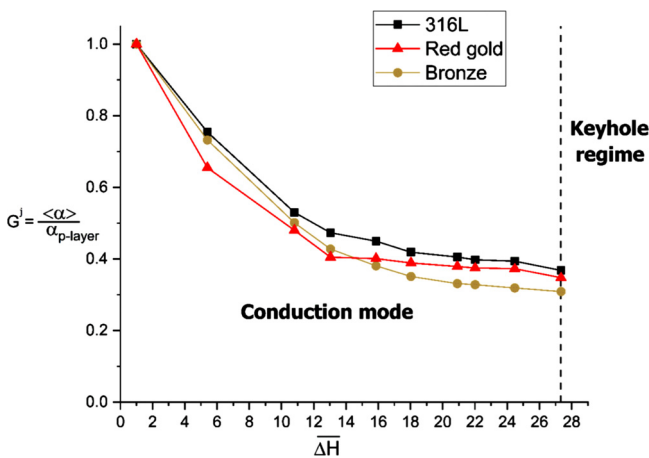

Fig. 14. The ratio of simulated effective powder absorptivity to powder layer measured absorptivity, G^j, versus normalized enthalpy for bronze, red gold, and 316 L steel, in the conduction mode. The vertical dotted line corresponds to the optimal $\Delta \bar{H}$, i.e. the near keyhole threshold.

the importance of the powder absorptivity and light penetration inside the powder bed. Furthermore, the effective absorptivity of the material is following the same trend as the powder layer absorptivity, for different values of the normalized enthalpy, in the conduction mode. These results demonstrate that using the room temperature powder layer absorptivity for translating parameters from one material to another in SLM is valid.

(4) The generality of the translation rule has been checked by considering three different materials and two different laser spot sizes.

Further studies are ongoing in order to check the sensitivity of the model to $\Delta \bar{H}$ variations for different materials. The proposed translation rule will be further investigated by looking at the sample size and at geometrical effects. In addition, an improvement in the finite element formulation will consider the light propagation in all three directions, as the current model only considers a propagation along the depth (z) direction. 3D propagation could be based on ray tracing models [63,64].

The proposed translation rule does not take into account all details of the SLM process (and many are important); however, it was demonstrated to be a powerful approach to translate the optimal parameters from one material to another, using straightforward measurements.

CRediT authorship contribution statement

Hossein Ghasemi-Tabasi: Conceptualization, Methodology, Validation, Software, Formal analysis, Investigation, Writing - original draft, Writing - review & editing, Data curation. **Jamasp Jhabvala:** Conceptualization, Methodology, Software, Validation, Formal analysis, Writing - review & editing, Supervision. **Eric Boillat:** Software, Formal analysis, Writing - review & editing. **Toni Ivas:** Software, Formal analysis, Writing - review & editing. **Rita Drissi-Daoudi:** Methodology, Validation, Formal analysis. **Roland E. Logé:** Conceptualization, Supervision, Project administration, Funding acquisition, Writing - review & editing.

Declaration of Competing Interest

None.

Acknowledgments

Appendix A. Supplementary data

Supplementary material related to this article can be found, in the online version, at doi:https://doi.org/10.1016/j.addma.2020.101496.

References

[1] G.N. Levy, R. Schindel, J.P. Kruth, Rapid manufacturing and rapid tooling with layer manufacturing (LM) technologies, state of the art and future perspectives, CIRP Ann. - Manuf. Technol. 52 (2003) 589–609, https://doi.org/10.1016/S0007-8506(07)60206-6.

[2] J. Mutua, S. Nakata, T. Onda, Z. Chen, Optimization of selective laser melting parameters and in fl uence of post heat treatment on microstructure and mechanical properties of maraging steel, Mater. Des. 139 (2018) 486–497, https://doi.org/10.1016/j.matdes.2017.11.042.

[3] E. Liverani, S. Toschi, L. Ceschini, A. Fortunato, Effect of selective laser melting (SLM) process parameters on microstructure and mechanical properties of 316L austenitic stainless steel, J. Mater. Process. Tech. 249 (2017) 255–263, https://doi.org/10.1016/j.jmatprotec.2017.05.042.

[4] W.M. Tucho, V.H. Lysne, H. Austbø, A. Sjolyst-kverneland, Investigation of effects of process parameters on microstructure and hardness of SLM manufactured SS316L, J. Alloys Compd. 740 (2018) 910–925, https://doi.org/10.1016/j.jallcom.2018.01.098.

[5] M. Tang, P.C. Pistorius, J.L. Beuth, Prediction of lack-of-fusion porosity for powder bed fusion, Addit. Manuf. 14 (2017) 39–48, https://doi.org/10.1016/j.addma.2016.12.001.

[6] B. Zhang, Y. Li, Q. Bai, Defect Formation Mechanisms in Selective Laser Melting: A Review, Chinese J. Mech. Eng. 30 (2017) 515–527, https://doi.org/10.1007/s10033-017-0121-5.

[7] F. Cooper, Sintering And Additive Manufacturing: The New Paradigm for the Jewelry Manufacturer, Proc. St. Fe Symp. Jewel. Manuf. Technol. (2012) 103–122.

[8] P.A.M. Damiano Zito, Silvano Bortolamei, Alessio Carlotto, Ilaria Cristofolini, Alessandro Loggi, Latest developments in Selective Laser Melting production of gold jewellery, St. Fe Symp., 2012, pp. 1–18.

[9] B.J. Fischer-buehner, P. Poliero, R. Bertoncello, A. Basso, L.G.S. A, J. Fischer-buehner, P. Poliero, R. Bertoncello, A. Basso, M. Poliero, Rapid Jewelry Manufacturing By Laser Melting of Precious Metal Powders (PLM): Fiction Or Future? Proc. St. Fe Symp. Jewel. Manuf. Technol. (2011) 177–202.

[10] D. Zito, A. Carlotto, A. Loggi, P. Sbornicchia, D. Maggian, S.A. Progold, T. Vi, M. Fockele, P. Unterberg, Optimization of the Main Selective Laser Melting Technology Parameters in the Production of Precious Metal Jewelry, Proc. St. Fe Symp. Jewel. Manuf. Technol. (2013) 1–20.

[11] U.E. Klotz, D. Tiberto, F. Held, Optimization of 18-karat yellow gold alloys for the additive manufacturing of jewelry and watch parts, Gold Bull. 50 (2017) 111–121, https://doi.org/10.1007/s13404-017-0201-4.

[12] U.E. Klotz, D. Tiberto, F. Held, U.E. Klotz, D. Tiberto, F. Held, Additive Manufacturing of 18-Karat Yellow-Gold alloys, Jewel. Technol. Forum 2 (2017).

[13] M. Khan, P. Dickens, Selective Laser Melting (SLM) of pure gold, Gold Bull. 43 (2010) 114–121, https://doi.org/10.1007/BF03214976.

[14] U. Scipioni Bertoli, A.J. Wolfer, M.J. Matthews, J.P.R. Delplanque, J.M. Schoenung, On the limitations of Volumetric Energy Density as a design parameter for Selective Laser Melting, Mater. Des. 113 (2017) 331–340, https://doi.org/10.1016/j.matdes.2016.10.037.

[15] S. Ghouse, S. Babu, R.J. Van Arkel, K. Nai, P.A. Hooper, J.R.T. Jeffers, The influence of laser parameters and scanning strategies on the mechanical properties of a stochastic porous material, Mater. Des. 131 (2017) 498–508, https://doi.org/10.1016/j.matdes.2017.06.041.

[16] L. Quintino, A. Costa, R. Miranda, D. Yapp, V. Kumar, C.J. Kong, Welding with high power fiber lasers - A preliminary study, Mater. Des. 28 (2007) 1231–1237, https://doi.org/10.1016/j.matdes.2006.01.009.

[17] J.J.S. Dilip, S. Zhang, C. Teng, K. Zeng, C. Robinson, D. Pal, B. Stucker, Influence of processing parameters on the evolution of melt pool, porosity, and microstructures in Ti-6Al-4V alloy parts fabricated by selective laser melting, Prog. Addit. Manuf. 2 (2017) 157–167, https://doi.org/10.1007/s40964-017-0030-2.

[18] A. Keshavarzkermani, E. Marzbanrad, R. Esmaeilizadeh, Y. Mahmoodkhani, U. Ali, P.D. Enrique, N.Y. Zhou, A. Bonakdar, E. Toyserkani, An investigation into the effect of process parameters on melt pool geometry, cell spacing, and grain refinement during laser powder bed fusion, Opt. Laser Technol. 116 (2019) 83–91, https://doi.org/10.1016/j.optlastec.2019.03.012.

[19] C. Zhao, K. Fezzaa, R.W. Cunningham, H. Wen, F. De Carlo, L. Chen, A.D. Rollett, T. Sun, Real-time monitoring of laser powder bed fusion process using high-speed X-ray imaging and diffraction, Sci. Rep. 7 (2017) 3602, https://doi.org/10.1038/s41598-017-03761-2.

[20] R. Cunningham, C. Zhao, N. Parab, C. Kantzos, J. Pauza, K. Fezzaa, T. Sun, A.D. Rollett, Keyhole threshold and morphology in laser melting revealed by ultrahigh-speed x-ray imaging, Science (80-.) 363 (2019) 849–852, https://doi.org/10.1126/science.aav4687.

[21] E. Soylemez, High deposition rate approach of selective laser melting through defocused single bead experiments and thermal finite element analysis for Ti-6Al-4V, Addit. Manuf. 31 (2020) 100984, https://doi.org/10.1016/j.addma.2019.100984.

[22] J. Metelkova, Y. Kinds, K. Kempen, C. de Formanoir, A. Witvrouw, B. Van Hooreweder, On the influence of laser defocusing in Selective Laser Melting of 316L, Addit. Manuf. 23 (2018) 161–169, https://doi.org/10.1016/j.addma.2018.08.006.

[23] M.F.A.J.C. Ion, H.R. Shercliff, Diagrams for laser materials processing, Acta Met, Mater. 40 (1992) 1539–1551.

[24] R. Rai, J.W. Elmer, T.A. Palmer, T. Debroy, Heat transfer and fluid flow during keyhole mode laser welding of tantalum, Ti-6Al-4V, 304L stainless steel and vanadium, J. Phys. D. Appl. Phys. 40 (2007) 5753–5766, https://doi.org/10.1088/0022-3727/40/18/037.

[25] D.W. Bäuerle, Laser Processing and Chemistry, 4th ed., Springer-Verlag, Berlin Heidelberg, 2011, https://doi.org/10.1007/978-3-642-17613-5.

[26] T.C. Chawla, D.L. Graff, R.C. Borg, G.L. Bordner, D.P. Weber, D. Miller, Thermophysical properties of mixed oxide fuel and stainless steel type 316 for use in transition phase analysis, Nucl. Eng. Des. 67 (1981) 57–74, https://doi.org/10.1016/0029-5493(81)90155-2.

[27] D.B. Hann, J. Iammi, J. Folkes, A simple methodology for predicting laser-weld properties from material and laser parameters, J. Phys. D. Appl. Phys. 44 (2011), https://doi.org/10.1088/0022-3727/44/44/445401.

[28] P. Promoppatum, S.C. Yao, Analytical evaluation of defect generation for selective laser melting of metals, Int. J. Adv. Manuf. Technol. 103 (2019) 1185–1198, https://doi.org/10.1007/s00170-019-03500-z.

[29] A.M. Kiss, A.Y. Fong, N.P. Calta, V. Thampy, A.A. Martin, P.J. Depond, J. Wang, M.J. Matthews, R.T. Ott, C.J. Tassone, K.H. Stone, M.J. Kramer, A. van Buuren, M.F. Toney, J. Nelson Weker, Laser-Induced Keyhole Defect Dynamics during Metal Additive Manufacturing, Adv. Eng. Mater. 21 (2019) 1–7, https://doi.org/10.1002/adem.201900455.

[30] W.E. King, H.D. Barth, V.M. Castillo, G.F. Gallegos, J.W. Gibbs, D.E. Hahn, C. Kamath, A.M. Rubenchik, Observation of keyhole-mode laser melting in laser powder-bed fusion additive manufacturing, J. Mater. Process. Technol. 214 (2014) 2915–2925, https://doi.org/10.1016/j.jmatprotec.2014.06.005.

[31] X. Jian, C.S. Wu, G. Zhang, J. Chen, A unified 3D model for an interaction mechanism of the plasma arc, weld pool and keyhole in plasma arc welding, J. Phys. D. Appl. Phys. 48 (2015), https://doi.org/10.1088/0022-3727/48/46/465504.

[32] S. Elena-manuela, U.T. Brasov, O. Dontu, Mechanism of keyhole formation and stability instationary laser welding, J. Phys. D. Appl. Phys. 35 (2002) 1570–1576.

[33] M. Rasch, C. Roider, S. Kohl, J. Strauß, N. Maurer, K.Y. Nagulin, M. Schmidt,

[34] E. Assuncao, S. Williams, D. Yapp, Interaction time and beam diameter effects on the conduction mode limit, Opt. Lasers Eng. 50 (2012) 823–828, https://doi.org/10.1016/j.optlaseng.2012.02.001.

[35] A.M. Rubenchik, W.E. King, S.S. Wu, Scaling laws for the additive manufacturing, J. Mater. Process. Tech. 257 (2018) 234–243, https://doi.org/10.1016/j.jmatprotec.2018.02.034.

[36] J. Ye, S.A. Khairallah, A.M. Rubenchik, M.F. Crumb, G. Guss, J. Belak, M.J. Matthews, Energy Coupling Mechanisms and Scaling Behavior Associated with Laser Powder Bed Fusion Additive Manufacturing, Adv. Eng. Mater. 1900185 (2019) 1–9, https://doi.org/10.1002/adem.201900185.

[37] R. Fabbro, Scaling laws for the laser welding process in keyhole mode, J. Mater. Process. Tech. 264 (2019) 346–351, https://doi.org/10.1016/j.jmatprotec.2018.09.027.

[38] M. Thomas, G.J. Baxter, I. Todd, Normalised model-based processing diagrams for additive layer manufacture of engineering alloys, Acta Mater. 108 (2016) 26–35, https://doi.org/10.1016/j.actamat.2016.02.025.

[39] L. Johnson, M. Mahmoudi, B. Zhang, R. Seede, X. Huang, J.T. Maier, H.J. Maier, I. Karaman, A. Elwany, A. Arróyave, Assessing printability maps in additive manufacturing of metal alloys, Acta Mater. 176 (2019) 199–210, https://doi.org/10.1016/j.actamat.2019.07.005.

[40] Z.H. Shen, S.Y. Zhang, J. Lu, X.W. Ni, Mathematical modeling of laser induced heating and melting in solids, 33 (2001), pp. 533–537.

[41] C.D. Boley, S.A. Khairallah, A.M. Rubenchik, Calculation of laser absorption by metal powders in additive manufacturing, Appl. Opt. 54 (2015) 2477, https://doi.org/10.1364/AO.54.002477.

[42] D. Sowdari, P. Majumdar, Finite element analysis of laser irradiated metal heating and melting processes, Opt. Laser Technol. 42 (2010) 855–865, https://doi.org/10.1016/j.optlastec.2009.11.022.

[43] X.C. Wang, T. Laoui, J. Bonse, J.P. Kruth, B. Lauwers, L. Froyen, Direct Selective Laser Sintering of Hard Metal Powders: Experimental Study and Simulation, Int. J. Adv. Manuf. Technol. 19 (2002) 351–357, https://doi.org/10.1007/s001700200024.

[44] P. Meakin, R. Jullien, Restructuring effects in the rain model for random deposition, J. Phys. 48 (1987) 1651–1662.

[45] Y.H. Zhou, Z.H. Zhang, Y.P. Wang, G. Liu, S.Y. Zhou, Y.L. Li, J. Shen, M. Yan, Selective laser melting of typical metallic materials: An effective process prediction model developed by energy absorption and consumption analysis, Addit. Manuf. 25 (2019) 204–217, https://doi.org/10.1016/j.addma.2018.10.046.

[46] J. Trapp, A.M. Rubenchik, G. Guss, M.J. Matthews, In situ absorptivity measurements of metallic powders during laser powder-bed fusion additive manufacturing, Appl. Mater. Today. 9 (2017) 341–349, https://doi.org/10.1016/j.apmt.2017.08.006.

[47] O. Loebich, The optical properties of gold, Gold Bull. 5 (1972) 2–10, https://doi.org/10.1007/BF03215148.

[48] J.N. Hodgson, The optical properties of gold, J. Phys. Chem. Solids. 29 (1968) 2175–2181, https://doi.org/10.1016/0022-3697(68)90013-9.

[49] Mark Fox, Optical Properties of Solids, Second Edi, Oxford University Press, Oxford, United Kingdom, 2010.

[50] C. Deng, J. Kang, T. Feng, Y. Feng, X. Wang, P. Wu, Study on the selective laser melting of CuSn10 powder, Materials (Basel). 11 (2018) 1–7, https://doi.org/10.3390/ma11040614.

[51] S. Scudino, C. Unterdörfer, K.G. Prashanth, H. Attar, N. Ellendt, V. Uhlenwinkel, J. Eckert, Additive manufacturing of Cu-10Sn bronze, Mater. Lett. 156 (2015) 202–204, https://doi.org/10.1016/j.matlet.2015.05.076.

[52] J. Ye, A.M. Rubenchik, M.F. Crumb, G. Guss, M.J. Matthews, Laser Absorption and Scaling Behavior in Powder Bed Fusion Additive Manufacturing of Metals, Conf. Lasers Electro-Optics, Optical Society of America, San Jose, California (2018) p. JW2A.117.

[53] H.G. Kim, W.R. Kim, O. Kwon, G.B. Bang, M.J. Ham, H.-K. Park, K.-H. Jung, K.M. Kim, C.-W. Lee, G.-H. Kim, Laser beam melting process based on complete-melting energy density for commercially pure titanium, J. Manuf. Process. 45 (2019) 455–459, https://doi.org/10.1016/j.jmapro.2019.07.031.

[54] J. Zhang, D. Gu, Y. Yang, H. Zhang, H. Chen, D. Dai, K. Lin, Influence of Particle Size on Laser Absorption and Scanning Track Formation Mechanisms of Pure Tungsten Powder during Selective Laser Melting, Engineering (2019), https://doi.org/10.1016/j.eng.2019.07.003.

[55] D. Moser, S. Pannala, J. Murthy, Computation of Effective Thermal Conductivity of Powders for Selective Laser Sintering Simulations, J. Heat Transfer. 138 (2016) 1–9, https://doi.org/10.1115/1.4033351.

[56] N. Sakatani, K. Ogawa, Y. Iijima, M. Arakawa, R. Honda, S. Tanaka, Thermal conductivity model for powdered materials under vacuum based on experimental studies, AIP Adv. 7 (2017), https://doi.org/10.1063/1.4975153.

[57] J. Yin, H. Zhu, L. Ke, P. Hu, C. He, H. Zhang, X. Zeng, A finite element model of thermal evolution in laser micro sintering, Int. J. Adv. Manuf. Technol. 83 (2016) 1847–1859, https://doi.org/10.1007/s00170-015-7609-x.

[58] S.A. Khairallah, A. Anderson, Mesoscopic simulation model of selective laser melting of stainless steel powder, J. Mater. Process. Technol. 214 (2014) 2627–2636, https://doi.org/10.1016/j.jmatprotec.2014.06.001.

[59] U. Scipioni Bertoli, G. Guss, S. Wu, M.J. Matthews, J.M. Schoenung, In-situ characterization of laser-powder interaction and cooling rates through high-speed imaging of powder bed fusion additive manufacturing, Mater. Des. 135 (2017) 385–396, https://doi.org/10.1016/j.matdes.2017.09.044.

[60] J. Jhabvala, Study of the consolidation process under macro- and microscopic

thermal effects in selective laser sintering and selective laser melting, EPFL PP - Lausanne, n.d. doi:10.5075/epfl-thesis-4609.

[61] J. Mingear, B. Zhang, D. Hartl, A. Elwany, Effect of process parameters and electropolishing on the surface roughness of interior channels in additively manufactured nickel-titanium shape memory alloy actuators, Addit. Manuf. 27 (2019) 565–575, https://doi.org/10.1016/j.addma.2019.03.027.

[62] K.-E. Peiponen, T. Tsuboi, Metal surface roughness and optical reflectance, Opt. Laser Technol. 22 (1990) 127–130, https://doi.org/10.1016/0030-3992(90) 90022-V.

[63] A.V. Gusarov, I. Yadroitsev, P. Bertrand, I. Smurov, Model of Radiation and Heat Transfer in Laser-Powder Interaction Zone at Selective Laser Melting, J. Heat Transfer. 131 (2009) 072101, , https://doi.org/10.1115/1.3109245.

[64] A.V. Gusarov, J.P. Kruth, Modelling of radiation transfer in metallic powders at laser treatment, Int. J. Heat Mass Transf. 48 (2005) 3423–3434, https://doi.org/10.1016/j.ijheatmasstransfer.2005.01.044.

[65] Y. Tokura, Optical and magnetic properties of transition metal oxides, Curr. Opin. Solid State Mater. Sci. 3 (1998) 175–180, https://doi.org/10.1016/S1359-0286(98) 80085-5.

[66] S.D. Jadhav, J. Vleugels, J.-P. Kruth, J. Van Humbeeck, K. Vanmeensel, Mechanical and electrical properties of selective laser-melted parts produced from surface-oxidized copper powder, Mater. Des. Process. Commun. (2019) e94, https://doi.org/10.1002/mdp2.94 0.

[67] T. Polivnikova, Study and Modelling of the Melt Pool Dynamics during Selective Laser Sintering and Melting, EPFL PP - Lausanne, n.d. doi:10.5075/epfl-thesis-6826.

[68] E. Boillat, Finite element methods on non-conforming grids by penalizing the matching constraint, ESAIM M2AN. 37 (2003) 357–372, https://doi.org/10.1051/m2an:2003031.

[69] D. Bergström, The Absorption of Laser Light by Rough Metal Surfaces, Luleå University of Technology, 2008.

[70] R. Glardon, N. Karapatis, V. Romano, Influence of Nd: YAG parameters on the selective laser sintering of metallic powders, CIRP Ann. - Manuf. Technol. 50 (2001) 133–136, https://doi.org/10.1016/S0007-8506(07)62088-5.

[71] J. Jhabvala, E. Boillat, R. Glardon, On the use of EBSD analysis to investigate the microstructure of gold samples built by selective laser melting, Gold Bull. 44 (2011) 113–118, https://doi.org/10.1007/s13404-011-0017-6.

[72] M. Schmid, S. Zehnder, P. Schwaller, B. Neuenschwander, M. Held, U. Hunziker, J. Zürcher, Measuring optical properties on rough and liquid metal surfaces, Proc ALT12. (2012), https://doi.org/10.12684/alt.1.78.

[73] K. Shankar, Thermophysical and optical property measurements of electro-magnetically-leviated liquid metals, Rice University, 1989.

[74] M. Salcudean, M. Choi, R. Greif, A study of heat transfer during arc welding, Int. J. Heat Mass Transf. 29 (1986) 215–225, https://doi.org/10.1016/0017-9310(86) 90229-2.

[75] Y. Yang, M.F. Knol, F. van Keulen, C. Ayas, A semi-analytical thermal modelling approach for selective laser melting, Addit. Manuf. 21 (2018) 284–297, https://doi.org/10.1016/j.addma.2018.03.002.

[76] A. Plotkowski, M.M. Kirka, S.S. Babu, Verification and validation of a rapid heat transfer calculation methodology for transient melt pool solidification conditions in powder bed metal additive manufacturing, Addit. Manuf. 18 (2017) 256–268, https://doi.org/10.1016/j.addma.2017.10.017.

[77] R. Miller, T. DebRoy, Energy absorption by metal-vapor-dominated plasma during carbon dioxide laser welding of steels, J. Appl. Phys. 68 (1990) 2045–2050, https://doi.org/10.1063/1.346555.

[78] Y. Tian, D. Tomus, P. Rometsch, X. Wu, Influences of processing parameters on surface roughness of Hastelloy X produced by selective laser melting, Addit. Manuf. 13 (2017) 103–112, https://doi.org/10.1016/j.addma.2016.10.010.

[79] B. Fotovvati, S.F. Wayne, G. Lewis, E. Asadi, A Review on Melt-Pool Characteristics in Laser Welding of Metals, Adv. Mater. Sci. Eng. 2018 (2018), https://doi.org/10.1155/2018/4920718.

[80] T. Polivnikova, Study and modelling of the melt pool dynamics during Selective Laser Sintering and Melting, 6826 (2015), p. 107.

[81] Copper alloys, PX Group, (n.d.). https://www.pxgroup.com/sites/default/files/CuSn8_1.pdf.

[82] Copper-tin and Copper-tin-zinc casting alloys (Tin bronze), (2017) https://www.kupferinstitut.de/wp-content/uploads/2019/09/Infodruck-i.-25.pdf.

[83] UNS C52100 (CW453K) Phosphor Bronze, (2019) https://www.makeitfrom.com/material-properties/UNS-C52100-CW453K-Phosphor-Bronze.

[84] EN CC480K (CuSn10-C) Tin Bronze, (2018) https://www.makeitfrom.com/material-properties/EN-CC480K-CuSn10-C-Tin-Bronze.

[85] E. ToolBox, Solids - Melting and Boiling Temperatures, (2003) https://www.engineeringtoolbox.com/melting-points-solids-d_148.html.

[86] K red gold 5N, for universal use, PX Group, (n.d.). https://www.pxgroup.com/sites/default/files/0518.pdf.

[87] P. Sbornicchia, S. Rappo, D. Zito, V. Doppio, F. Tiso, G. Cepeda, S.A. Progold, Understanding Gold Alloy Features From Thermodynamic Phenomena, St. Fe Symp. Jewel. Manuf. Technol. 39 (2018) 517–560.

[88] C.S. Kim, Thermophysical properties of stainless steels, United States, (1975) http://inis.iaea.org/search/search.aspx?orig_q=RN:07236394.

[89] T. Heeling, M. Cloots, K. Wegener, Melt pool simulation for the evaluation of process parameters in selective laser melting, Addit. Manuf. 14 (2017) 116–125, https://doi.org/10.1016/j.addma.2017.02.003.

[90] C.L.A. Leung, S. Marussi, M. Towrie, R.C. Atwood, P.J. Withers, P.D. Lee, The effect of powder oxidation on defect formation in laser additive manufacturing, Acta Mater. 166 (2019) 294–305, https://doi.org/10.1016/j.actamat.2018.12.027.

[91] S.A. Khairallah, A.A. Martin, J.R.I. Lee, G. Guss, N.P. Calta, J.A. Hammons, M.H. Nielsen, K. Chaput, E. Schwalbach, M.N. Shah, M.G. Chapman, T.M. Willey, A.M. Rubenchik, A.T. Anderson, Y.M. Wang, M.J. Matthews, W.E. King, Controlling interdependent meso-nanosecond dynamics and defect generation in metal 3D printing, Science (80-.) 368 (2020) 660–665, https://doi.org/10.1126/science.aay7830.

[92] T. DebRoy, H.L. Wei, J.S. Zuback, T. Mukherjee, J.W. Elmer, J.O. Milewski, A.M. Beese, A. Wilson-Heid, A. De, W. Zhang, Additive manufacturing of metallic components – Process, structure and properties, Prog. Mater. Sci. 92 (2018) 112–224, https://doi.org/10.1016/j.pmatsci.2017.10.001.

[93] B.J. Simonds, J. Sowards, J. Hadler, E. Pfeif, B. Wilthan, J. Tanner, C. Harris, P. Williams, J. Lehman, Time-Resolved Absorptance and Melt Pool Dynamics during Intense Laser Irradiation of a Metal, Phys. Rev. Appl. 10 (2018) 1, https://doi.org/10.1103/PhysRevApplied.10.044061.

[94] C. Van Gestel, Study of physical phenomena of selective laser melting towards increased productivity, EPFL, 2015, https://doi.org/10.5075/epfl-thesis-6817.